Parametric Model to Analyze the Components of the Thermal Conductivity of a Cellulose-Nanofibril Aerogel

Masanao Obori, Donguk Suh, Shunsuke Yamasaki, Takashi Kodama, Tsuguyuki Saito, Akira Isogai, and Junichiro Shiomi

Phys. Rev. Applied **11**, 024044 — Published 19 February 2019

DOI: 10.1103/PhysRevApplied.11.024044

Parametric Model to Analyze Components of Cellulose Nanofibril Aerogel Thermal Conductivity

Masanao Obori[1], Donguk Suh[1], Shunsuke Yamasaki[2], Takashi Kodama[1], Tsuguyuki Saito[2], Akira Isogai[2], and Junichiro Shiomi[1,3,]*

[1]Department of Mechanical Engineering, the University of Tokyo, 7-3-1 Hongo, Bunkyo-ku, Tokyo 113-8656, Japan.

[2]Department of Biomaterial Sciences, the University of Tokyo, 1-1-1 Yayoi, Bunkyo-ku, Tokyo 113-8657, Japan.

[3]Center for Materials research by Information Integration, National Institute for Materials Science, 1-2-1 Sengen, Tsukuba, Ibaraki 305-0047, Japan

Corresponding Author

*Junichiro Shiomi. Email: shiomi@photon.t.u-tokyo.ac.jp. Tel: +81-3-5841-6283.

ABSTRACT

Cellulose nanofibril aerogels have been found to be a highly effective thermal insulator, where some reports state that they have lower thermal conductivity than air. To further enhance the

performance of the material, it is important to understand the contribution of the three heat transfer components: solid heat conduction by the fibrils, gas heat conduction by the Knudsen gas in pores, and thermal radiation between the fibrils. In this work, the overall effective thermal conductivity was measured by an in-house steady-state setup under atmospheric and vacuum conditions. Contributions from each heat transfer component were quantified by constructing a simple open-cell model and fitting it to the experimental measurements, which varied based on the solid volume fraction. The thermal conductivity values of a single cellulose nanofibril filament that constitutes the struts of the open cell structure were well within the range of previous studies, which confirms the validity of the analysis results. The analysis model was extended to reveal target dimensions when fabricating aerogels that will provide minimum thermal conductivity. All in all, the simple analysis method can be further applied to improve other porous thermal insulation materials.

KEYWORDS: cellulose nanofibril aerogel, open-cell model, thermal conductivity, parameter optimization

PACS number(s): 44.30.+v, 44.10.+i , 44.05.+e

I. INTRODUCTION

The necessity of insulation materials is primarily to conserve energy by decreasing heat transfer through interfaces. The divide in temperatures provided by insulation has numerous industrial and environmental benefits and therefore has been studied extensively in physics, chemistry, and materials science[1-4]. Among the materials, cellulose nanofibril (CNF) aerogels

have gathered great interest because of their thermal and mechanical properties that originate from their configurational characteristics[5-14]. There have been many studies on using cellulose as a new material since it is the most plentiful biopolymer on earth, biodegradable, relatively easy to manipulate, hydrophilic, mechanically stable, and has a thermal conductivity lower than air[15-17]. Similarly, aerogels are not only known to have good thermal insulating properties due to their high content of air, but also have extremely low densities, small pore sizes, and thus high surface areas[18-20]. Numerous studies have focused on combining cellulose with other species to form aerogel composites that have better mechanical stability while retaining optical and/or thermal properties favorable to be applied for insulation materials[21-27].

Bendahou et al.[24] used cellulose and a varied concentration of zeolite to tune the mechanical and thermal properties of the aerogel depending on the application. Fan et al.[25] created a CNF-AlOOH aerogel composite that not only was an effective insulator but also exhibited significant flame retardant properties. Jiang and Hsieh[28] modified CNF with methylene diphenyl diisocyanate changing the thermal and mechanical stability as well as the hydrophobicity. Focusing on the thermal transport aspect of CNF aerogels, various experiments have been conducted[29-32] and analytic models have been constructed[33, 34] to decompose the gas, solid, and radiative contributions on the thermal conductivity. Most of the experimental studies were only able to provide the overall effective thermal conductivity of the CNF aerogels they manufactured. Baillis et al.[33] constructed a thorough analytical model incorporating the gas contribution, skeletal porous structure, and radiative thermal conductivity. The model was able to recreate most of the experimental results but was constrained by the sophisticated input data from the experiments. Coquard and Baillis[34] simplified their previous model using a Kelvin cell

for their tetrakaidecahedron open-cell frame, but still, their results were highly dependent on intricate data from experiments.

The purpose of this study is to develop a simple and robust model that can reproduce the thermal conductivity of CNF aerogels obtained from experiments. Through the model, a full understanding of the quantitative contributions of gas, solid, and radiation component can be obtained. Therefore, an in-house heat flow meter was developed to measure the thermal conductivity of CNF aerogels having different solid volume fractions. The thermal conductivity measurements were conducted separately under atmospheric and vacuum conditions. Thereafter, an analytical model was made from basic geometry and heat transfer theories that will be explained in detail subsequently. Further details concerning the experimental setup and methodology will be described in the following section.

II. EXPERIMENTAL METHOD

The CNF aerogels measured in this study were fabricated by the methods incorporated in reference[29]. The samples were initially prepared by acid-induced gelation of a CNF dispersion, followed by solvent exchange from acidic water to ethanol, and finalized with supercritical CO_2 drying. Supercritical drying can avoid the collapse of aerogel structures during liquid removal by eliminating the liquid/vapor surface tension and thus attain structures with nanoporosity[31, 35, 36]. Details on how the thermal conductivity was measured will be stated thoroughly in the appendix.

A. Preparation of CNF aqueous dispersions

CNF is generally prepared from a softwood bleached kraft pulp. In this case, the pulp was chemically modified with a carboxyl group by mixing 2,2,6,6 tetramethylpiperidine-1-oxyl

(TEMPO) with water, sulfur bromide and sodium hypochlorite. The modified pulp then passed through a high-pressure water jet system (HJP-25001, Sugino Machine) five times thus concluding the defibrating process. The concentrations of the resulting CNF dispersions were adjusted by diluting with water or condensing with an evaporator under reduced pressure.

B. Supercritical CO_2 drying

Before supercritical drying is implemented, the CNF suspension is placed into a plastic mold and 1 mol/L of HCl is added and settled for 1h. Thereafter, a newly formed hydrogel is taken from the mold, shaken in a mixture of HCl and ethanol and then left to settle for 24 h. Then the hydrogel was cut with a sharp blade and shaken in ethanol for another 3 days, where the ethanol was refreshed twice a day. The resulting alcogels were placed in a chamber of a critical point dryer (SYSGLCP-8, Sanyu-Gijutsu) under a liquid CO_2 flow at 15℃ for 8 h. The chamber temperature was then increased to 40℃ to obtain the supercritical phase and maintained for 30 min after which the chamber was gradually depressurized for 1h.

C. Measuring thermal conductivity

The thermal conductivity was measured using a newly developed in-house heat flow meter by the guarded hot plate method[37]. This method applies guarded heating from the side of the test specimen to minimize heat loss from an electric input to measure the thermal conductivity. A new setup was necessary because of the small scale of the samples coupled with the demand for results from vacuum conditions. The schematic diagram, sensitivity results, and further details about the measurement method can be found in the appendix.

III. THEORETICAL MODEL

There are mainly three modes of heat transfer in an aerogel that affect the effective thermal conductivity κ_{eff}, which when neglecting any coupling can be decomposed as

$$\kappa_{eff} = \kappa_{gas} + \kappa_{solid} + \kappa_{radiation}$$ [38]. (1)

The thermal conductivity from conduction through gas and solid are κ_{solid} and κ_{gas}, respectively, whereas the radiation contribution is $\kappa_{radiation}$. Thermal convection can be disregarded for aerogels since gas flow, in general, cannot build up in such highly constricted confinements[39]. The methods of how each component was modeled will be explained in the following.

A. Thermal conductivity through gas

The most commonly used thermal conductivity model for gas for small pores is the Kaganer model, which considers the type of gas, pressure, temperature, and pore size[40]. The gas type can be combined with the pore size into the Knudsen number *Kn*, which gives

$$\kappa_g = \frac{\kappa_{g0}}{1+2\beta Kn} = \frac{\kappa_{g0}}{1+2\beta\Lambda/D}, \quad (2)$$

where

$$\Lambda = \frac{1}{\sqrt{2}\pi d_g^2 n_g} = \frac{k_B T}{\sqrt{2}\pi d_g^2 p} \quad (3)$$

and κ_{g0} is the thermal conductivity of the gas in free space, β is a coefficient dependent on the accommodation coefficient and the adiabatic gas coefficient, Λ the mean free path, D the characteristic length (pore size), d_g the molecular diameter, n_g the gas number density, k_B the Boltzmann constant, T the temperature, and p the pressure[41].

B. Thermal conductivity through solid

The solid conduction component for aerogels is lesser compared to dense bulk materials because the existence of pores inhibits phonon propagation through the solid frame[42]. Among the various methods to analytically calculate the thermal conductivity of solids, an open cell model is most appropriate because it resembles the skeletal structure of aerogels[43]. An open-cell model as in reference [43] was used to understand the heat transfer characteristics of the aerogel network and air. The model based on this simple cubic lattice (jungle gym) structure has a unit cell illustrated in the shaded areas of Fig. 1a and 1b. Half of the strut thickness, edge length, and thermal conductivity of the fiber, are t, L, and κ_s, respectively. Based on the configuration of the unit cell, four classifications can be made (Fig. 1c): ① full length of cellulose filament, ② crossbar of cellulose filament, ③ air entrapped between struts, ④ cuboid volume of air. The thermal resistance R of the four classifications can be written as

$$R_1 = \frac{L}{\kappa_s t^2},\ R_2 = \frac{2}{\kappa_s (L-2t)},\ R_3 = \frac{2}{\kappa_g t},\ R_4 = \frac{4L}{\kappa_g (L-2t)^2}, \tag{4}$$

where the total thermal resistance of one cell is

$$R_{framework} = \frac{4}{\kappa_{framework} L}$$

and the thermal network for the open cell can be found (Fig. 1d). Based on this network, the total thermal resistance becomes

$$R_{eff} = \frac{R_1 R_4 (2R_2 + R_3)}{2R_1 R_4 + (2R_2 + R_3)(R_1 + R_4)}.$$

Therefore, the structural characteristics of the thermal conductivity become

$$\kappa_{framework} = \frac{4\kappa_s t^2 + \kappa_g (L-2t)^2}{L^2} + \frac{4\kappa_s \kappa_g t^2 + \kappa_g (L-2t)t}{2L\kappa_g t + L\kappa_s (L-2t)}. \quad (5)$$

C. Radiative conductivity

Assuming CNF aerogels are optically thick, the spectral absorption coefficient and emission coefficient become equivalent based on Kirchhoff's law, and the Rosseland Approximation in the following equation can be used.

$$\kappa_{radiation} = \frac{16\sigma T^3}{3E_R} \quad (6)$$

Details on the derivation of Eq. (6) from the radiative transport equation can be found in reference [44], where σ and E_R, are the Stefan-Boltzmann constant and Rosseland mean extinction coefficient, respectively. E_R is related to the spectral extinction coefficient E_κ and Planck's Blackbody Distribution Law I_κ through

$$E_R^{-1} = \left[\int_0^\infty \frac{1}{E_\kappa} \cdot \frac{dI_\kappa(T)}{dT} d\kappa\right] \cdot \left[\int_0^\infty \frac{dI_\kappa(T)}{dT} d\kappa\right]^{-1} \quad (7)$$

for wavelength κ, where

$$E_\kappa = -\ln(\tau_\kappa)/t_{sample}. \quad (8)$$

In Eq. (8), t_{sample} is the sample thickness and τ_κ is the transmittance, which can be obtained through

$$\tau_\kappa = I_\kappa(T)\big|_L / I_\kappa(T)\big|_0. \quad (9)$$

Planck's law can be written as

$$I_\kappa(T) = \frac{C_1}{\kappa^5\left[\exp(C_2/\kappa T) - 1\right]} \ \text{W/m}^2\mu m, \quad (10)$$

where

$$C_1 = 2\pi hc_0^2 = 3.742\times10^8\ \mathrm{W}\cdot\mu\mathrm{m}^4/\mathrm{m}^2 \tag{11}$$

and

$$C_2 = hc_0/k_B = 1.439\times10^4\ \mu\mathrm{m}\times\mathrm{K}. \tag{12}$$

Here, h is the Planck constant and c_0 is the speed of light.

Consequently, in theory, the transmittance and thickness of the sample in Eq. (8) are the only experimental parameters required to obtain the Rosseland mean extinction coefficient and thus the radiative conductivity. Among the various models for foam materials to obtain E_R [45-47], Zhao et al.[48] and Dietrich et al.[44] used the following

$$E_R = C\frac{(1-\Pi)^n}{L}, \tag{13}$$

where L is the aforementioned edge length, C and n are parameters related to the material property. Π is the porosity, which is calculated by dividing the sum of the air volume (sections ③ and ④ in Fig. 1c) by the entire unit cell volume L^3 and becomes

$$\Pi = 16\left(\frac{t}{L}\right)^3 - 12\left(\frac{t}{L}\right)^2 + 1. \tag{14}$$

This is identical to the porosity model used in reference [49]. The strut half-length t, which is the edge length of a square in Eq. (13) and Fig. 1, was converted into the diameter of a circle that corresponded to the same area of the whole strut length ($2t$) by $4t/\sqrt{\pi}$ because the aforementioned models are for cylindrical struts.

The following section will explain how the theories are used to further understand the experimental results.

IV. RESULTS AND DISCUSSION

The experimental results of the thermal conductivity dependence on the volume fraction of the solid phase of cellulose for vacuum and atmosphere are plotted in Fig. 2a. A summary of the experimental values, gas contribution based on the decoupled model in Eq. (1), and corresponding porosities are in Table I. The vacuum measurements show a 30% increase in thermal conductivity from the volume fraction ranging from 0.3% to 1.4%, whereas the atmospheric results present a 28% decrease for the same range of the solid phase.

To further examine each mode contribution to the effective thermal conductivity in Eq. (1), Eqs. (2), (5), and (6) were combined. For vacuum and atmospheric conditions, $\kappa_{g0} = 0$ W·m^{-1}K^{-1} and κ_{g0}=0.026 W·m^{-1}K^{-1} are inserted into Eq. (2), respectively, where β is an open parameter. Previous transmission electron microscopic analyses[5, 29, 50] provided the strut diameter to be around 3.0 nm, so t was fixed to be 1.5 nm (since the open cell model uses half the strut thickness) and L was calculated by Eq. (14) and inserted into Eq. (5), where κ_s is also left as an open parameter. Two sets (atmospheric and vacuum) of open parameters exist for Eq. (13), which are labeled n_{atm}, n_{vac}, C_{atm}, and C_{vac}. After obtaining E_R from the parameters, it is substituted into Eq. (6). In summary, β, κ_s, n_{atm}, n_{vac}, C_{atm}, and C_{vac} are open parameters that are simultaneously obtained through optimization by minimizing the difference between the theoretical model and the experimental results, which are also stated in Table I. The Nelder-Mead simplex algorithm[51] was used for the minimization and a wide range of initial conditions were tested to avoid getting trapped in a local minimum. During the optimization process, some parameter combinations may exhibit a good fit even though they are not the global optimum. Details on the sensitivity of the fitting parameters will be presented in the appendix. A summary of the values of the predicted parameters is in Table II. The model does not completely mimic

the declining or ascending trends for the atmospheric and vacuum data points but quantitatively provides an adequate fit.

Due to time and material restraints, multiple measurements could not be conducted. Nevertheless, the aerogels that were measured have an isotropic skeleton and are soft in nature, so the possible innate uncertainty caused by imperfect contact between the hot plate and sample is minimal; moreover, the heat transferred through the framework is unlikely to show a significant variation due to its isotropic nature. Therefore, other studies show the thermal conductivity of cellulose aerogels to have error bars comparable with the symbol size[31, 35]. Based on a conservative sensitivity analysis explained in the appendix, the uncertainty of the theoretical model is expected to be within 15%.

A summary of the contributions of gas, solid, and radiation components of the effective conductivity for atmospheric and vacuum are in Table III, where the corresponding plot is Fig. 2b. The solid contribution can be acquired from the thermal conductivity for the framework in vacuum since there is no gas (κ_g=0) in $\kappa_{framework}$. The gas contribution κ_{gas} can be obtained by subtracting the solid contribution κ_{solid} from $\kappa_{framework}$ for atmospheric calculations. The solid contribution for atmospheric and vacuum are identical by definition. The increase in the amount of cellulose nanofibrils will naturally increase the solid contribution, and the results show that thermal energy transport through gas and radiative modes will decrease, where the decrease of radiation for atmospheric is more pronounced. The difference in vacuum and atmospheric heat transfer originates from disparate controlling modes, where the former is radiative heat transfer and the latter thermal conductivity through air. In both cases, atmospheric and vacuum, a fraction of energy will start favoring to travel through solid over radiation as its transport medium at

certain V_s values. Furthermore, the model slightly overestimates the gas contribution $\Delta\kappa_{eff\text{-}gas}$ compared with the indirectly obtained experimental result.

Through the parametric optimization methodology used in this study, experimentally unattainable parameters β and κ_s can be acquired as in Table II. Though the target material is cellulose nanofibril aerogels, the compared values in literature are the strands or some equivalent configuration from similar materials such as silica aerogels[46], cellulose thin films[34], or polyurethane foams[43, 47]. The κ_s values calculated through elaborate models or indirect estimations from the aforementioned studies are 0.25 $W{\cdot}m^{-1}K^{-1}$, 0.1 $W{\cdot}m^{-1}K^{-1}$, 0.5832 $W{\cdot}m^{-1}K^{-1}$, and 0.262 $W{\cdot}m^{-1}K^{-1}$, respectively. In comparison, more direct measurements on nanopaper[52] (~1.45 $W{\cdot}m^{-1}K^{-1}$) thin cellulose nanosheets[53] (~2.5 $W{\cdot}m^{-1}K^{-1}$) or actual single fibril simulations by DFT or molecular dynamics[54, 55] show κ_s to range from 0.9 to 5.7 $W{\cdot}m^{-1}K^{-1}$. The κ_s value found from a parametric fit in this study was 1.47 $W{\cdot}m^{-1}K^{-1}$, which is well in the range of other CNF studies. The parameter optimization used in this study actually provides a concrete method to consistently obtain the thermal conductivity of a single strand of solid in aerogels through experimental data, which is invaluable in analyzing and designing new materials. The model quantitatively exhibits how each component is affected by the V_s variation.

Additionally, most previous studies[5, 31] agree with the current results on cellulose aerogels showing an inverse proportionality on the effective thermal conductivity within the same range of solid volume fractions. Similar tendencies have also been previously reported for silica aerogels[46], which are also known to have a lower thermal conductivity than air[56-58].

After obtaining the optimal fit parameters, an extension in the range of V_s beyond the experimental data (V_s =1.4%) provides a minimum thermal conductivity of 23 ∓ 4 $mW{\cdot}m^{-1}K^{-1}$ around V_s =0.9% in Fig. 3a. This is an overestimation of the actual minimum value of 20.7

$mW \cdot m^{-1}K^{-1}$ and at a lower V_s than what was found from the experimental threshold of V_s =1.4%. Note that the difference in κ between 0.9 and 1.4 is less than 2% for the model, whereas the experimental data showed a difference to be approximately 15%. Based on the small variation in κ over a rather wide range of V_s predicted by the model, it is possible that the minimum resides in the region of V_s=0.9~1.4. This concave upward trend is not only qualitatively identical with that of Kobayashi et al.[5], but the solid volume fraction of the minimum thermal conductivity predicted by the model is also quantitatively close to that found from separate experiments. Studies that show increasing thermal conductivities with solid volume fractions are considered to be samples beyond the minimum when they were processed[29]. The minimum for the atmospheric data occurs due to a balance between more heat transfer choosing to pass through the filaments, thus reducing the transport of air and radiation, which is clearly displayed in Fig. 3b. The actual crossover of κ_{solid} becoming greater than κ_{gas} is at a V_s value higher than where the minimum occurs. The higher V_s beyond 1.4 is more difficult to manufacture aerogel configurations because of gelation characteristics. A gradual rise in κ is obtained for vacuum, which is purely due to the increase in the solid component.

The final analysis point considers different strut thicknesses (t was fixed at 1.5 nm up till now) for constant solid volume fractions. V_s =0.6 and 2.8 were examined and the results are illustrated in Fig. 4. No minimum could be found for a wide range of t values. From Fig. 4a, one can observe the thermal conductivity of vacuum crossing over the atmospheric value around t =7 nm for V_s =0.6 and around t =10 nm for V_s =2.8. If aerogels can be manufactured at such high solid volume fractions with the morphology being intact, the model predicts that fibrils can become thick enough to have a higher κ_{solid} than air. The gap between atmospheric and vacuum is smaller for the higher volume fraction overall. The decomposition plots in Fig. 4b shows the lower

volume fraction to have a smaller discrepancy between the components of atmospheric and vacuum compared to the higher situation in panel c, where the early dominance in the solid component for the latter is apparent. There is no variation for κ_{solid} because the solid volume fractions are kept constant, so the increase in κ due to strut thickness t, purely originates from the increase in radiation for vacuum. There is a slight increase in the gas contribution for atmospheric, but it is still modest compared with that of radiation based on this model. From all of the gathered results, the model can prescribe future CNF aerogels be fabricated around V_s=0.9% with the thinnest strut diameter possible in order to obtain the best insulation performance.

V. CONCLUSIONS

To understand how much heat is actually transferred through the air and solid within cellulose nanofibril aerogels, the thermal conductivity was measured by an in-house heat flow meter under atmospheric and vacuum conditions. The effective thermal conductivity in vacuum increased with the solid volume fraction because heat transport through nanofibers was the primary mode of energy transfer. In atmospheric conditions, a lower porosity was found to decrease the overall thermal conductivity since the amount of air within the aerogel decreased. For further insight into each heat transfer component, an open-cell model was constructed, and parameter optimization was performed. Through the model, the effective thermal conductivity was decomposed into the gas, solid, and radiative components. For both atmospheric and vacuum conditions, the radiative component clearly showed a higher contribution than heat transfer through the cellulose fibers, and transport through air exhibited the largest proportion for all modes and porosities. Furthermore, the thermal conductivity of a single cellulose nanofibril filament that constitutes the struts of the open cell structure, which is immeasurable, could be

obtained. The simple model and parameter optimization method applied to analyze CNF aerogels is promising for obtaining actual solid thermal conductivity of other cellulose composites and beyond.

ACKNOWLEDGMENTS

The authors thank Junko Morikawa for providing the reference samples and thermal conductivity data used for validating the developed thermal conductivity measurement setup. This work was partially supported by grants-in-aid for scientific research from Challenging Research (Exploratory) (Grant No. 17K18837) and Grant-in-Aid for Scientific Research (B) (Grant No. 16H04274 and 15H04524) from JSPS KAKENHI, Japan, and from CREST (Grant No. JPMJCR13B2) and Mirai programs of JST, Japan. DS was financially supported by JSPS postdoctoral fellowship P17068.

APPENDIX

1. DETAILS OF THERMAL CONDUCTIVITY MEASUREMENTS

The thermal conductivity κ was obtained from the heat flux Q measured by the sensor, where the thickness of the sample Δx and the temperature difference between the ends of the sample ΔT constitute

$$\kappa = \frac{Q\Delta x}{\Delta T}.$$

Therefore, the amount of heat loss from a test specimen directly correlates with the error in the conductivity measurements. To measure properties of insulation materials, the Japanese Industrial Standard requires a 300 mm×300 mm test section, but aerogels are difficult to manufacture in such large scales, so a 10 mm×10 mm test section was made and a micrometer

was attached to measure the thickness. The temperatures are measured by thermocouples. The newly developed device was inserted into a vacuum chamber, which was regulated at 0.40~0.63 Pa through a turbomolecular pump. This pressure has been reported to be sufficiently low enough to disregard any thermal conductivity from air[59]. A detailed schematic of the setup is in Fig. 5.

The thermal conductivity measurements were conducted after the heat flux stabilized. The setup was preprogrammed to recognize the stabilization, which provided convenience and consistency in making the measurements under steady-state conditions. Due to the minute scale of the samples and corresponding scale of the test section of this newly developed setup, the innate thermal resistance was large and heat loss into the atmosphere from wiring also became critical. This issue was circumvented by calibrating the output current of the sensor to stay in line with the ambient temperature.

Tables IV and V are benchmarks taken from standard materials showing little difference from nominal values or measurements from other established groups. The heat flux sensor used in our setup was from Captec, which is known to have an uncertainty of ∓3%. The comparison of thermal conductivity measurements in the benchmark for different materials is in Tables IV and V, where the difference is less than 2 $mW \cdot m^{-1}K^{-1}$ or 5%.

2. SENSITIVITY ANALYSIS OF PARAMETERS

The error bars in Fig. 3a represent 30% error bars that were used to conduct a sensitivity analysis of parameters. A normal distribution of 10,000 data points was randomly generated for each V_s value, where the range was within the error bars. Thermal conductivities corresponding to each V_s value for both atmospheric and vacuum (5 each) were randomly selected, and a

parametric fit was conducted for these sample data points. Figure 6 presents a histogram of the fitted parameters. Based on the results, one can see that κ_s is clearly the most sensitive parameter.

The resultant thermal conductivities from the parameters are plotted in Fig. 7. Most of the histograms fit well on a normal distribution as expected since the random sample originated from a normal distribution. The dashed region in Fig. 3a illustrates the error region (one standard deviation being around 15%) extrapolated to the higher V_s values. The dashed region falls well inside the 30% error bars, which means the sensitivity of this model is tolerable. Considering that the starting point of 30% error bars is conservative, one can reasonably conclude that the overall uncertainty of this method is well within the standard deviation values from Fig. 7 of approximately 15%.

REFERENCES

1 H. Abe, I. Abe, K. Sato, and M. Naito, Dry Powder Processing of Fibrous Fumed Silica Compacts for Thermal Insulation, Journal of the American Ceramic Society **88**, 1359 (2005).

2 H. Schwab, U. Heinemann, A. Beck, H. P. Ebert, and J. Fricke, Dependence of Thermal Conductivity on Water Content in Vacuum Insulation Panels with Fumed Silica Kernels, Journal of Building Physics **28**, 319 (2005).

3 R. Baetens, B. P. Jelle, and A. Gustavsen, Aerogel insulation for building applications: A state-of-the-art review, Energy and Buildings **43**, 761 (2011).

4 D. G. Cahill, W. K. Ford, K. E. Goodson, G. D. Mahan, A. Majumdar, H. J. Maris, R. Merlin, and S. R. Phillpot, Nanoscale thermal transport, Journal of Applied Physics **93**, 793 (2003).

5 Y. Kobayashi, T. Saito, and A. Isogai, Aerogels with 3D Ordered Nanofiber Skeletons of Liquid-Crystalline Nanocellulose Derivatives as Tough and Transparent Insulators, Angew. Chem. Int. Ed. **53**, 10394 (2014).

6 G. Hayase, K. Kanamori, K. Abe, H. Yano, A. Maeno, H. Kaji, and K. Nakanishi, Polymethylsilsesquioxane–Cellulose Nanofiber Biocomposite Aerogels with High Thermal Insulation, Bendability, and Superhydrophobicity, ACS Applied Materials & Interfaces **6**, 9466 (2014).

[7] J. H. Park, J. Noh, C. Schutz, G. Salazar-Alvarez, G. Scalia, L. Bergstrom, and J. P. F. Lagerwall, Macroscopic Control of Helix Orientation in Films Dried from Cholesteric Liquid-Crystalline Cellulose Nanocrystal Suspensions, ChemPhysChem **15**, 1477 (2014).

[8] I. Usov, G. Nystrom, J. Adamcik, S. Handschin, C. Schutz, A. Fall, L. Bergstrom, and R. Mezzenga, Understanding nanocellulose chirality and structure-properties relationship at the single fibril level, Nature Communications **6**, 7564 (2015).

[9] M. Licen, B. Majaron, J. Noh, C. Schutz, L. Bergstrom, J. Lagerwall, and I. Drevensek-Olenik, Correlation between structural properties and iridescent colors of cellulose nanocrystalline films, Cellu **23**, 3601 (2016).

[10] P. Munier, K. Gordeyeva, L. Bergstrom, and A. B. Fall, Directional Freezing of Nanocellulose Dispersions Aligns the Rod-Like Particles and Produces Low-Density and Robust Particle Networks, Biomacromolecules **17**, 1875 (2016).

[11] S. Lee, K. Y. Kang, M. J. Jeong, A. Potthast, and F. Liebner, Evaluation of Supercritical CO2 Dried Cellulose Aerogels as Nano-Biomaterials, Journal of the Korean Physical Society **71**, 483 (2017).

[12] N. Pircher, L. Carbajal, C. Schimper, M. Bacher, H. Rennhofer, J. M. Nedelec, H. C. Lichtenegger, T. Rosenau, and F. Liebner, Impact of selected solvent systems on the pore and solid structure of cellulose aerogels, Cellu **23**, 1949 (2016).

[13] D. Ciolacu, C. Rudaz, M. Vasilescu, and T. Budtova, Physically and chemically cross-linked cellulose cryogels: Structure, properties and application for controlled release, Carbohydr. Polym. **151**, 392 (2016).

[14] E. Guilminot, R. Gavillon, M. Chatenet, S. Berthon-Fabry, A. Rigacci, and T. Budtova, New nanostructured carbons based on porous cellulose: Elaboration, pyrolysis and use as platinum nanoparticles substrate for oxygen reduction electrocatalysis, Journal of Power Sources **185**, 717 (2008).

[15] Y. Zhang, T. Nypelö, C. Salas, J. Arboleda, I. C. Hoeger, and O. J. Rojas, Cellulose Nanofibrils, Journal of Renewable Materials **1**, 195 (2013).

[16] N. Lavoine and L. Bergstrom, Nanocellulose-based foams and aerogels: processing, properties, and applications, Journal of Materials Chemistry A **5**, 16105 (2017).

[17] N. Pircher, S. Veigel, N. Aigner, J. M. Nedelec, T. Rosenau, and F. Liebner, Reinforcement of bacterial cellulose aerogels with biocompatible polymers, Carbohydr. Polym. **111**, 505 (2014).

[18] H. Zheng, H. Shan, Y. Bai, X. Wang, L. Liu, J. Yu, and B. Ding, Assembly of silica aerogels within silica nanofibers: towards a super-insulating flexible hybrid aerogel membrane, RSC Adv. **5**, 91813 (2015).

[19] S. Spagnol, B. Lartigue, A. Trombe, and V. Gibiat, Modeling of thermal conduction in granular silica aerogels, J. Sol-Gel Sci. Technol. **48**, 40 (2008).

[20] U. Heinemann, R. Caps, and J. Fricke, Radiation-conduction interaction: an investigation on silica aerogels, International Journal of Heat and Mass Transfer **39**, 2115 (1996).

[21] S. S. Nair, P. Y. Kuo, H. Y. Chen, and N. Yan, Investigating the effect of lignin on the mechanical, thermal, and barrier properties of cellulose nanofibril reinforced epoxy composite, Industrial Crops and Products **100**, 208 (2017).

[22] U. M. Garusinghe, S. Varanasi, G. Garnier, and W. Batchelor, Strong cellulose nanofibre-nanosilica composites with controllable pore structure, Cellu **24**, 2511 (2017).

[23] N. Saba, F. Mohammad, M. Pervaiz, M. Jawaid, O. Y. Alothman, and M. Sain, Mechanical, morphological and structural properties of cellulose nanofibers reinforced epoxy composites, Int. J. Biol. Macromol. **97**, 190 (2017).
[24] D. Bendahou, A. Bendahou, B. Seantier, Y. Grohens, and H. Kaddami, Nano-fibrillated cellulose-zeolites based new hybrid composites aerogels with super thermal insulating properties, Industrial Crops and Products **65**, 374 (2015).
[25] B. T. Fan, S. J. Chen, Q. F. Yao, Q. F. Sun, and C. D. Jin, Fabrication of Cellulose Nanofiber/AlOOH Aerogel for Flame Retardant and Thermal Insulation, Materials **10**, 311 (2017).
[26] D. Gebauer, V. Oliynyk, M. Salajkova, J. Sort, Q. Zhou, L. Bergstrom, and G. Salazar-Alvarez, A transparent hybrid of nanocrystalline cellulose and amorphous calcium carbonate nanoparticles, Nanoscale **3**, 3563 (2011).
[27] A. Demilecamps, C. Beauger, C. Hildenbrand, A. Rigacci, and T. Budtova, Cellulose-silica aerogels, Carbohydr. Polym. **122**, 293 (2015).
[28] F. Jiang and Y. L. Hsieh, Cellulose Nanofibril Aerogels: Synergistic Improvement of Hydrophobicity, Strength, and Thermal Stability via Cross-Linking with Diisocyanate, Acs Applied Materials & Interfaces **9**, 2825 (2017).
[29] K. Sakai, Y. Kobayashi, T. Saito, and A. Isogai, Partitioned airs at microscale and nanoscale: thermal diffusivity in ultrahigh porosity solids of nanocellulose, Scientific Reports **6**, 20434 (2016).
[30] P. L. Hurtado, A. Rouilly, V. Vandenbossche, and C. Raynaud, A review on the properties of cellulose fibre insulation, Build. Environ. **96**, 170 (2016).
[31] C. Jimenez-Saelices, B. Seantier, B. Cathala, and Y. Grohens, Spray freeze-dried nanofibrillated cellulose aerogels with thermal superinsulating properties, Carbohydr. Polym. **157**, 105 (2017).
[32] J. Chen, X. Y. Huang, Y. K. Zhu, and P. K. Jiang, Cellulose Nanofiber Supported 3D Interconnected BN Nanosheets for Epoxy Nanocomposites with Ultrahigh Thermal Management Capability, Advanced Functional Materials **27**, 1604754 (2017).
[33] D. Baillis, R. Coquard, and L. M. Moura, Heat transfer in cellulose-based aerogels: Analytical modelling and measurements, Energy **84**, 732 (2015).
[34] R. Coquard and D. Baillis, Thermal conductivity of Kelvin cell cellulosic aerogels: analytical and Monte Carlo approaches, Journal of Materials Science **52**, 11135 (2017).
[35] F. Fischer, A. Rigacci, R. Pirard, S. Berthon-Fabry, and P. Achard, Cellulose-based aerogels, Polymer **47**, 7636 (2006).
[36] C. Zhang, Y. Wang, and S. L. Liu, A facile pathway for the incorporation of silica into cellulose aerogels with increased optical transmittance, Materials Technology **31**, 549 (2016).
[37] T. Kobari, J. Okajima, A. Komiya, and S. Maruyama, Development of guarded hot plate apparatus utilizing Peltier module for precise thermal conductivity measurement of insulation materials, International Journal of Heat and Mass Transfer **91**, 1157 (2015).
[38] M. Aegerter, Leventis, N., Koebel, M. M. , *Aerogels Handbook* (Springer New York, 2011).
[39] L. W. Hrubesh and R. W. Pekala, Thermal properties of organic and inorganic aerogels, J. Mater. Res. **9**, 731 (1994).
[40] M. G. Kaganer, *Thermal Insulation in Cryogenic Engineering* (Israel Program for Scientific Translations, 1969).

[41] S. Q. Zeng, A. Hunt, and R. Greif, Transport properties of gas in silica aerogel, Journal of Non-Crystalline Solids **186**, 264 (1995).
[42] C. Jiménez-Saelices, B. Seantier, B. Cathala, and Y. Grohens, Spray freeze-dried nanofibrillated cellulose aerogels with thermal superinsulating properties, Carbohydr. Polym. **157**, 105 (2017).
[43] K. Ankang and H. Houde, Effective Thermal Conductivity of Open Cell Polyurethane Foam Based on the Fractal Theory, Advances in Materials Science and Engineering **2013**, 125267 (2013).
[44] B. Dietrich, T. Fischedick, S. Heissler, P. G. Weidler, C. Wöll, and M. Kind, Optical parameters for characterization of thermal radiation in ceramic sponges – Experimental results and correlation, International Journal of Heat and Mass Transfer **79**, 655 (2014).
[45] R. A. Campo-Arnáiz, M. A. Rodríguez-Pérez, B. Calvo, and J. A. de Saja, Extinction coefficient of polyolefin foams, J. Polym. Sci., Part B: Polym. Phys. **43**, 1608 (2005).
[46] G. Wei, Y. Liu, X. Zhang, F. Yu, and X. Du, Thermal conductivities study on silica aerogel and its composite insulation materials, International Journal of Heat and Mass Transfer **54**, 2355 (2011).
[47] M. Wang and N. Pan, Modeling and prediction of the effective thermal conductivity of random open-cell porous foams, International Journal of Heat and Mass Transfer **51**, 1325 (2008).
[48] C. Y. Zhao, T. J. Lu, and H. P. Hodson, Thermal radiation in ultralight metal foams with open cells, International Journal of Heat and Mass Transfer **47**, 2927 (2004).
[49] J.-S. Kwon, C. H. Jang, H. Jung, and T.-H. Song, Effective thermal conductivity of various filling materials for vacuum insulation panels, International Journal of Heat and Mass Transfer **52**, 5525 (2009).
[50] T. Saito, T. Uematsu, S. Kimura, T. Enomae, and A. Isogai, Self-aligned integration of native cellulose nanofibrils towards producing diverse bulk materials, Soft Matter **7**, 8804 (2011).
[51] J. C. Lagarias, J. A. Reeds, M. H. Wright, and P. E. Wright, Convergence Properties of the Nelder-Mead Simplex Method in Low Dimensions, SIAM Journal of Optimization **9**, 112 (1998).
[52] X. Zeng, J. Sun, Y. Yao, R. Sun, J.-B. Xu, and C.-P. Wong, A Combination of Boron Nitride Nanotubes and Cellulose Nanofibers for the Preparation of a Nanocomposite with High Thermal Conductivity, ACS Nano **11**, 5167 (2017).
[53] K. Uetani, T. Okada, and H. T. Oyama, Crystallite Size Effect on Thermal Conductive Properties of Nonwoven Nanocellulose Sheets, Biomacromolecules **16**, 2220 (2015).
[54] J. A. Diaz, Z. Ye, X. Wu, A. L. Moore, R. J. Moon, A. Martini, D. J. Boday, and J. P. Youngblood, Thermal Conductivity in Nanostructured Films: From Single Cellulose Nanocrystals to Bulk Films, Biomacromolecules **15**, 4096 (2014).
[55] L. D. Fernando, S. ShunLi, G. H. Louis, Jr., S. Paul, L. Zi-Kui, J. M. Robert, and D. Z. Pablo, Anisotropy and temperature dependence of structural, thermodynamic, and elastic properties of crystalline cellulose I β : a first-principles investigation, Modell. Simul. Mater. Sci. Eng. **22**, 085012 (2014).
[56] Y. Zhao, G. H. Tang, and M. Du, Numerical study of radiative properties of nanoporous silica aerogel, International Journal of Thermal Sciences **89**, 110 (2015).
[57] S. Q. Zeng, A. Hunt, and R. Greif, Geometric Structure and Thermal Conductivity of Porous Medium Silica Aerogel, Journal of Heat Transfer **117**, 1055 (1995).

[58] T. Xie, Y.-L. He, and Z.-J. Hu, Theoretical study on thermal conductivities of silica aerogel composite insulating material, International Journal of Heat and Mass Transfer **58**, 540 (2013).

[59] D. Ganta, E. B. Dale, J. P. Rezac, and A. T. Rosenberger, Optical method for measuring thermal accommodation coefficients using a whispering-gallery microresonator, The Journal of Chemical Physics **135**, 084313 (2011).

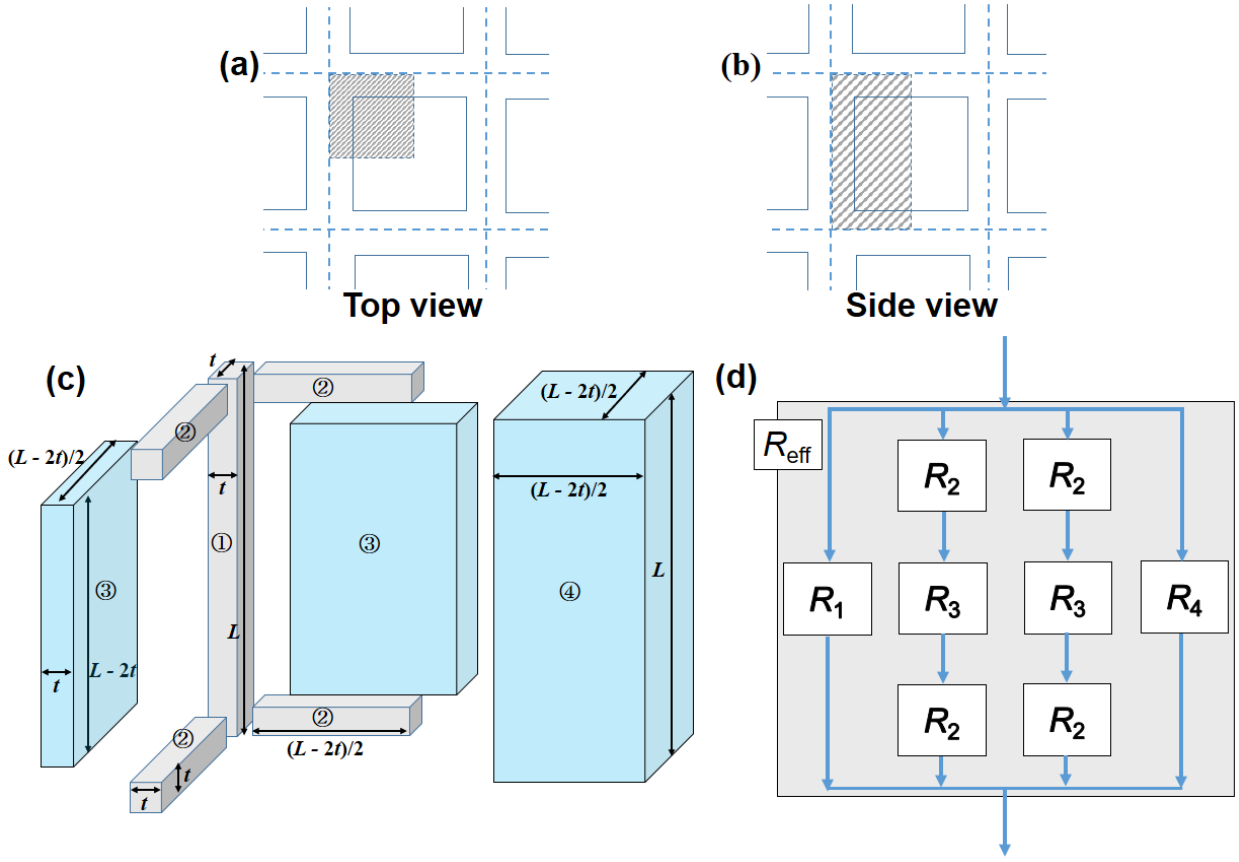

FIG 1. Viewpoints of a unit cell from the (a) top and (b) side. (c) Four classifications of volumes within the unit cell, where heat transfer will occur. (d) Thermal network scheme.

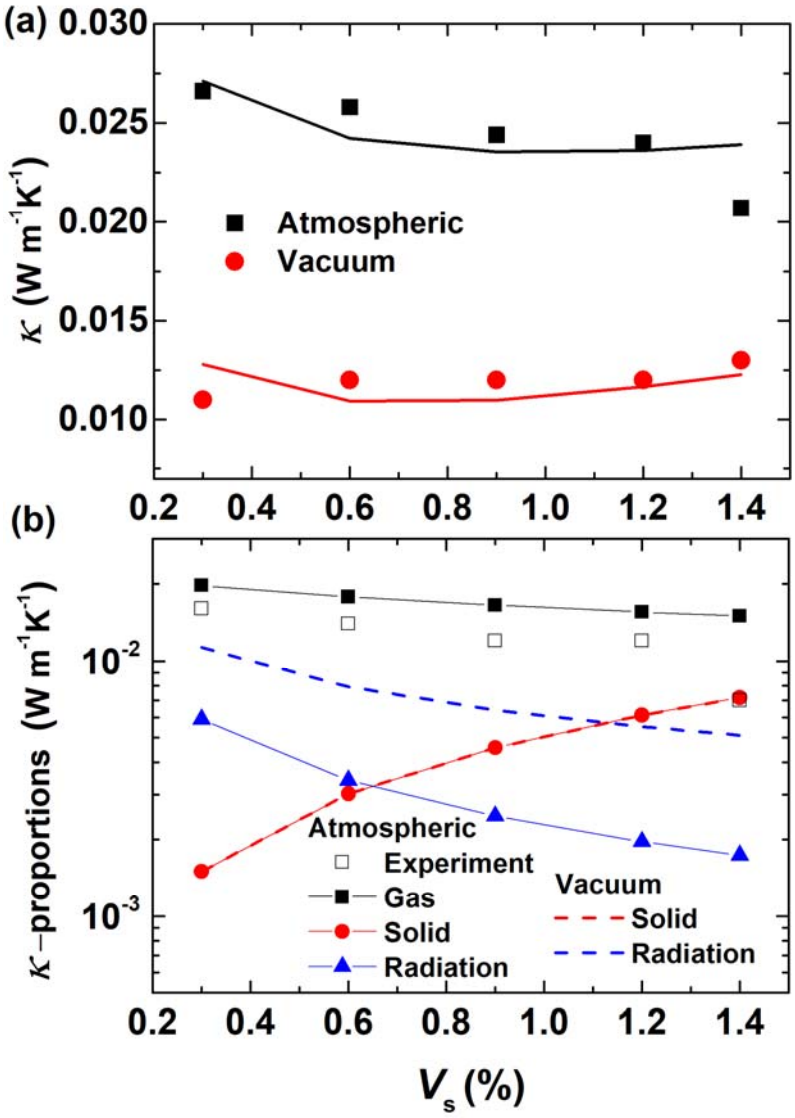

FIG 2. (a) Thermal conductivity for different solid volume fractions from experiments and the theoretical model. The symbols are for the former, whereas the lines are the latter. (b) Thermal conductivity proportions for gas, solid, and radiation components for atmospheric and vacuum conditions and $\Delta\kappa_{\text{eff-}gas}$ in Table I.

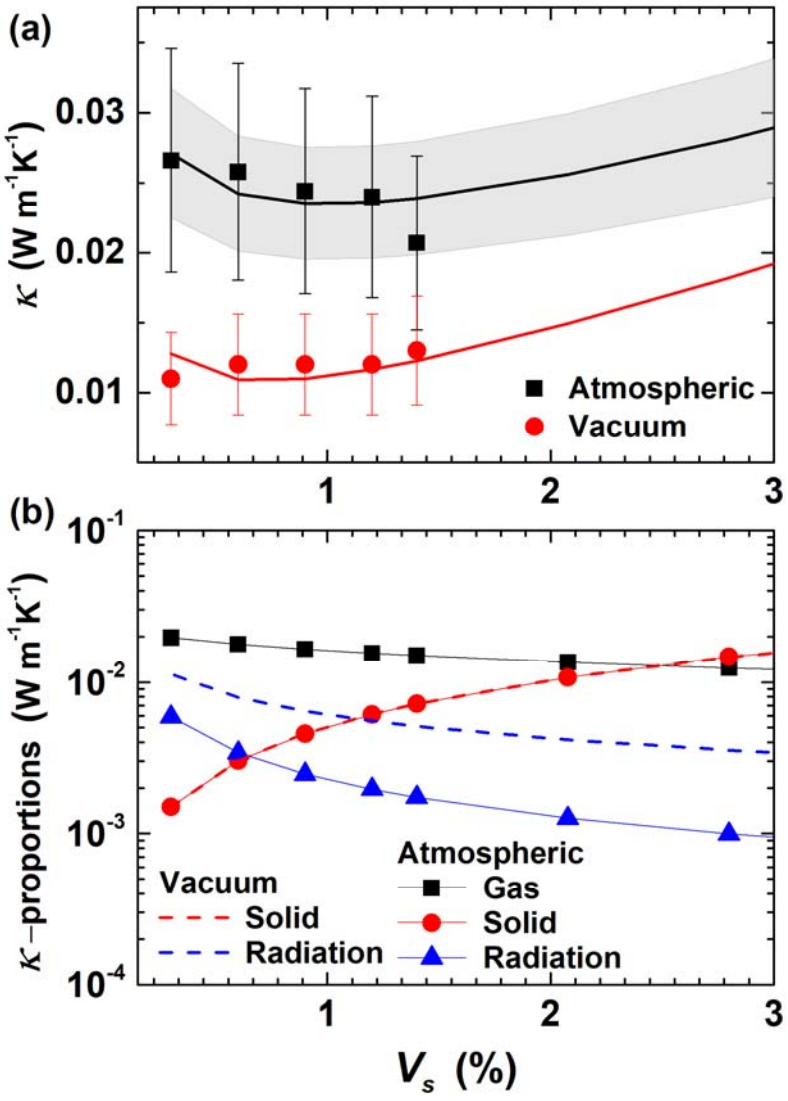

FIG. 3. Expanded plots of Fig. 2 over the values of V_s. (a) Thermal conductivity for different solid volume fractions from experiments and the theoretical model. The symbols are for the former, whereas the lines are the latter. The dashed region is the uncertainty from the model. (b) Thermal conductivity proportions of the gas, solid, and radiation components for atmospheric and vacuum conditions.

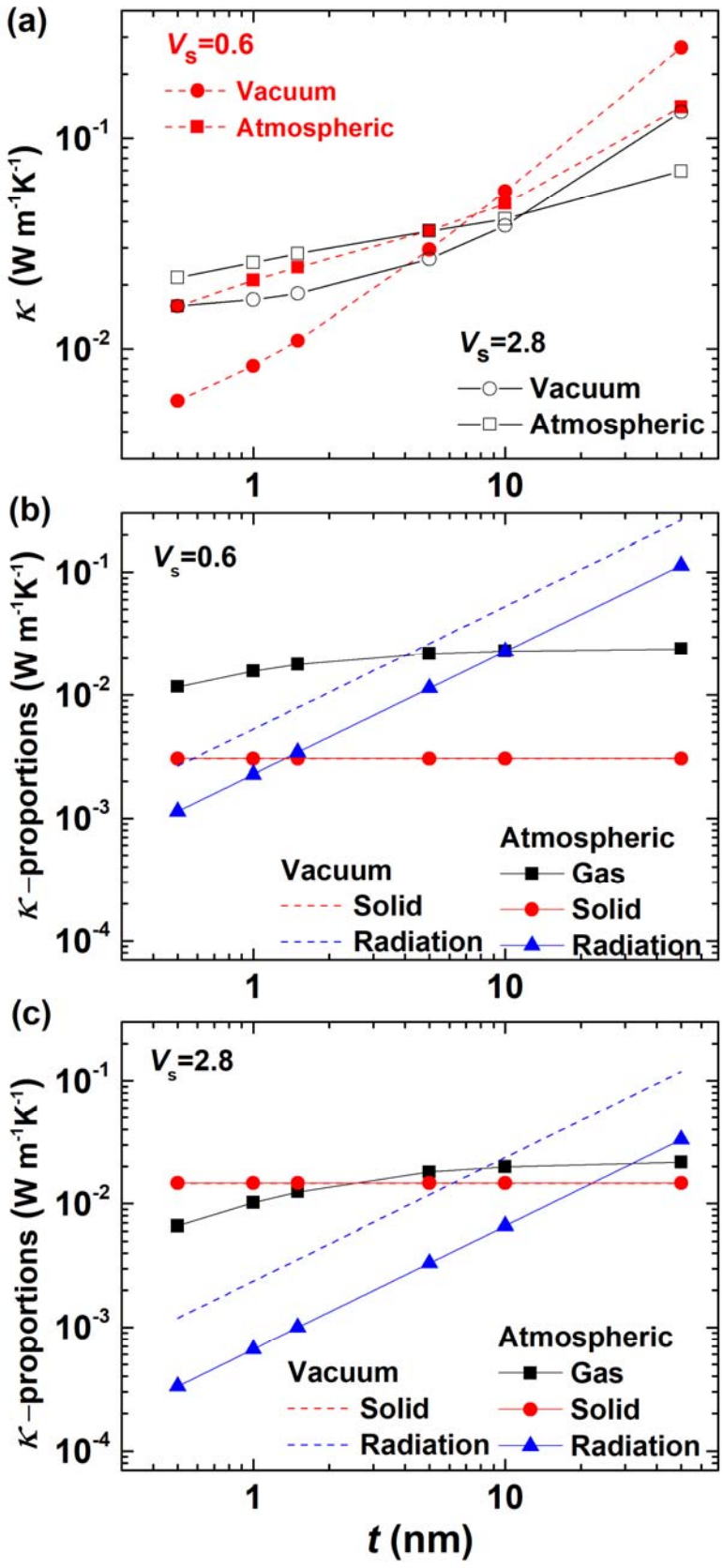
(a)
V_s=0.6
Vacuum
Atmospheric
V_s=2.8
Vacuum
Atmospheric
κ (W m^{-1}K^{-1})
(b)
V_s=0.6
Vacuum
Solid
Radiation
Atmospheric
Gas
Solid
Radiation
κ–proportions (W m^{-1}K^{-1})
(c)
V_s=2.8
Vacuum
Solid
Radiation
Atmospheric
Gas
Solid
Radiation
κ–proportions (W m^{-1}K^{-1})
t (nm)

FIG. 4. (a) Thermal conductivity for constant solid volume fractions from the theoretical model. (b) Thermal conductivity proportions of the gas, solid, and radiation components for atmospheric and vacuum conditions for V_s=0.6 and (c) V_s=2.8.

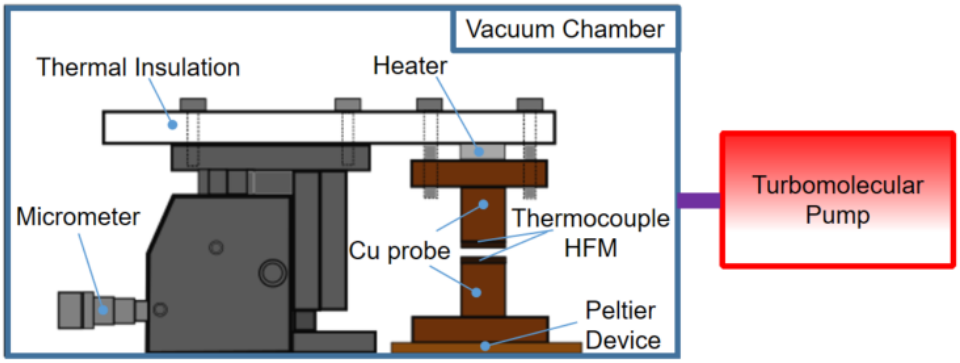

FIG. 5. Schematic of experimental setup.

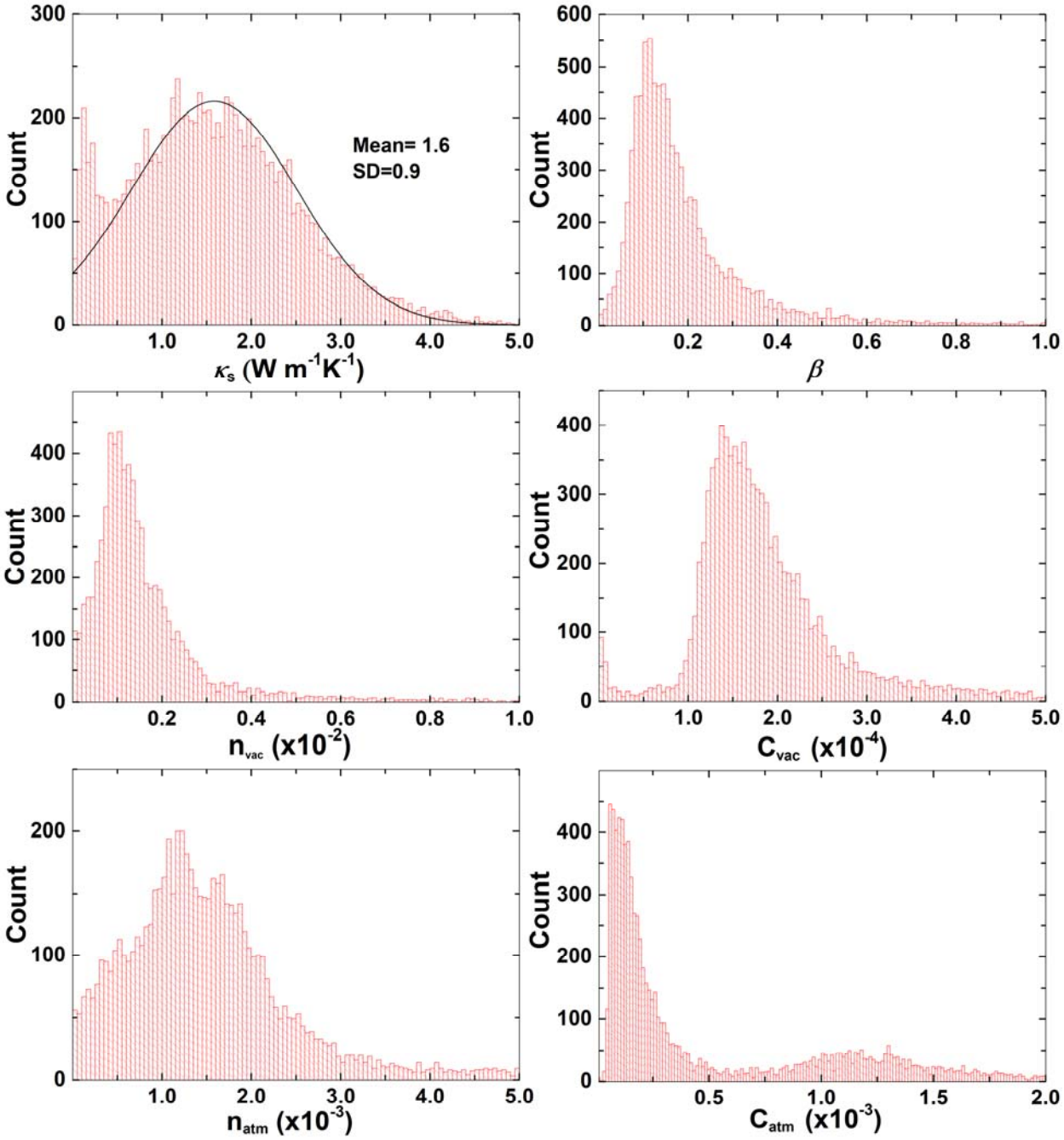

FIG. 6 Histogram of fitting parameters evaluated for sensitivity analysis

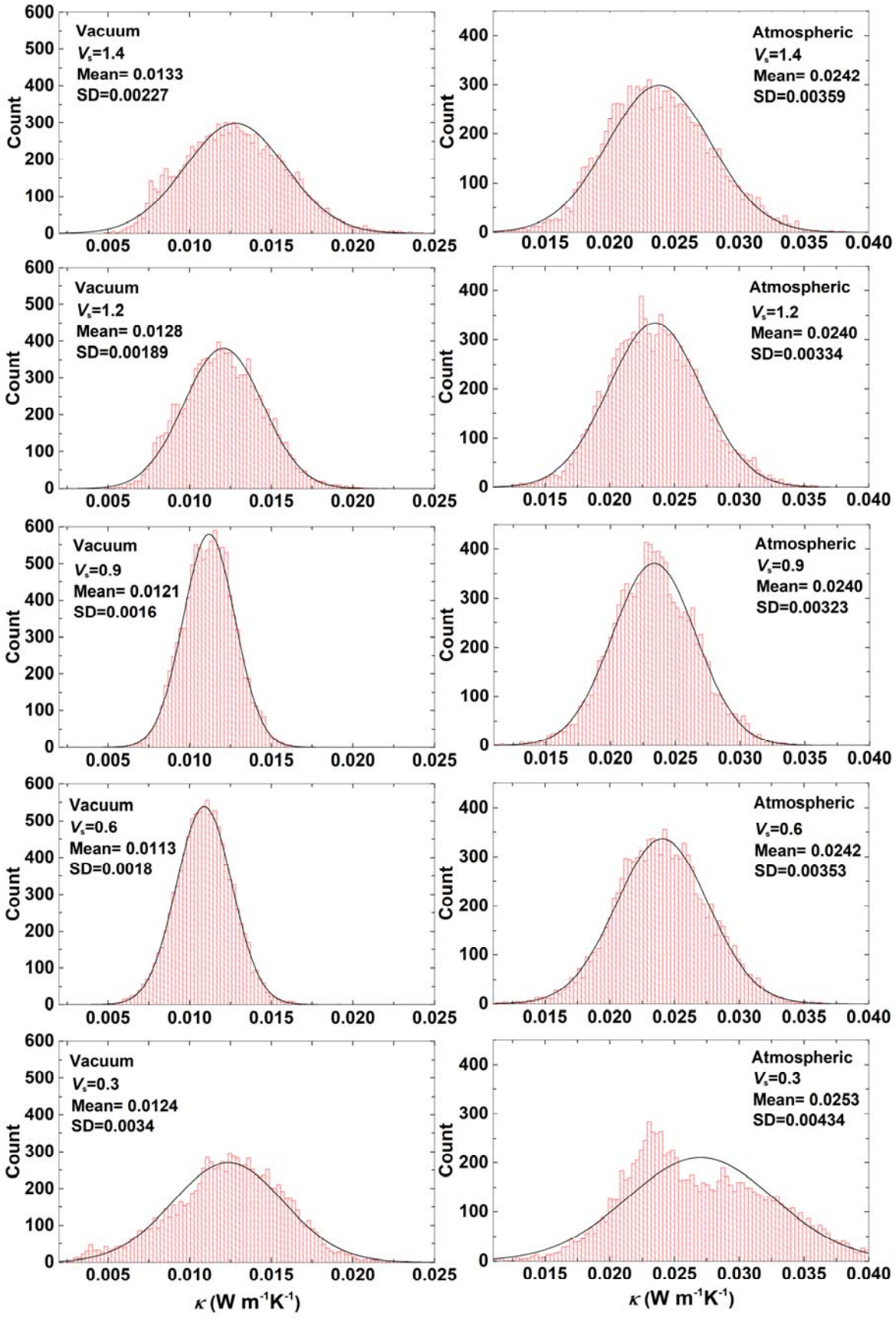
Vacuum
V_s=1.4
Mean= 0.0133
SD=0.00227
Atmospheric
V_s=1.4
Mean= 0.0242
SD=0.00359
Vacuum
V_s=1.2
Mean= 0.0128
SD=0.00189
Atmospheric
V_s=1.2
Mean= 0.0240
SD=0.00334
Vacuum
V_s=0.9
Mean= 0.0121
SD=0.0016
Atmospheric
V_s=0.9
Mean= 0.0240
SD=0.00323
Vacuum
V_s=0.6
Mean= 0.0113
SD=0.0018
Atmospheric
V_s=0.6
Mean= 0.0242
SD=0.00353
Vacuum
V_s=0.3
Mean= 0.0124
SD=0.0034
Atmospheric
V_s=0.3
Mean= 0.0253
SD=0.00434
Count
κ (W m^{-1}K^{-1})

FIG. 7. Histogram and normal distribution curves (SD: standard deviation) of resultant thermal conductivity values from random parameter assignment.

Table I. A summary of the experimental results, model fit, gas conductivity from experiments, and porosity Π.

V_s (%)	Atmospheric $\kappa_{eff\text{-}atm}$(W·m^{-1}K^{-1})		Vacuum $\kappa_{eff\text{-}vac}$(W·m^{-1}K^{-1})		$\Delta\kappa_{eff\text{-}gas}$ (W·m^{-1}K^{-1}) = $\Delta\kappa_{eff\text{-}atm}$ - $\Delta\kappa_{eff\text{-}vac}$	Π
	Experiment	Model	Experiment	Model		
0.3	0.0266	0.0271	0.011	0.0128	0.016	0.997
0.6	0.0258	0.0242	0.012	0.0109	0.014	0.994
0.9	0.0244	0.0236	0.012	0.0110	0.012	0.991
1.2	0.0240	0.0236	0.012	0.0117	0.012	0.988
1.4	0.0207	0.0239	0.013	0.0123	0.007	0.986

Table II. Parameter values from the optimal fit.

κ_s [W m^{-1} K^{-1}]	1.47
β [-]	0.108
n_{vac} [-]	7.36x10^{-3}
C_{vac} [-]	1.81x10^{-4}
n_{atm} [-]	2.86x10^{-1}
C_{atm} [-]	1.59x10^{-3}

Table III. A summary of the proportions of thermal conductivities calculated from the aforementioned theories in section III. Unless mentioned, all units are (W·m^{-1}K^{-1}).

	Atmospheric			Vacuum	
V_s (%)	κ_{gas}	κ_{solid}	$\kappa_{radiation}$	κ_{solid}	$\kappa_{radiation}$
0.3	1.97×10^{-2}	1.50×10^{-3}	5.90×10^{-2}	1.50×10^{-3}	1.13×10^{-2}
0.6	1.78×10^{-2}	3.02×10^{-3}	3.41×10^{-3}	3.02×10^{-3}	7.91×10^{-2}
0.9	1.65×10^{-2}	4.57×10^{-3}	2.47×10^{-3}	4.57×10^{-3}	6.42×10^{-2}
1.2	1.55×10^{-2}	6.13×10^{-3}	1.96×10^{-3}	6.13×10^{-3}	5.53×10^{-2}
1.4	1.50×10^{-2}	7.18×10^{-3}	1.74×10^{-3}	7.18×10^{-3}	5.11×10^{-2}

Table IV. Commercial rock wool (Nichias) thermal conductivity measurements for atmospheric and vacuum (0.63 Pa) conditions.

	Measured	Nominal
Atmospheric ($W\cdot m^{-1}K^{-1}$)	0.044 (80 g/cm^3)	0.042 (86 g/cm^3)
Vacuum ($W\cdot m^{-1}K^{-1}$)	0.011 (80 g/cm^3)	0.013 (166 g/cm^3)

Table V. Thermal conductivity measurements in atmosphere for expanded polystyrene (EPS) and melamine sponge. The benchmark values are measurements taken from Junko Morikawa's group at the Tokyo Institute of Technology. All units are ($mW\cdot m^{-1}K^{-1}$) unless otherwise stated.

	Measured	Benchmark
EPS (60 kg/m^3)	42.0	40.0
EPS (46 kg/m^3) NIST	38.0	38.0
EPS (20 kg/m^3)	34.0	33.5
Melamine sponge	32.0	31.5